Supplement of Atmos. Chem. Phys., 23, 15325–15350, 2023
https://doi.org/10.5194/acp-23-15325-2023-supplement
© Author(s) 2023. CC BY 4.0 License.

Atmospheric Chemistry and Physics
Open Access
EGU

Supplement of

Investigating the contribution of grown new particles to cloud condensation nuclei with largely varying preexisting particles – Part 1: Observational data analysis

Xing Wei et al.

Correspondence to: Xiao-Ying Yu (yuxiaoying@ornl.gov) and Xiaohong Yao (xhyao@ouc.edu.cn)

The copyright of individual parts of the supplement might differ from the article licence.

Supplementary text legends:

S1 Operational details of experiments

S2 Calculation methods

S3 Inter-comparison of particle number concentration related instruments

S4 Artifact analysis of N_{ccn} and κ values at lab-calibrated SS and approximated on-site SS

Figure legends:

Fig. S1 Temporal variations in relative humidity (RH, a) and temperature (T, b) from 29 June to 15 July 2019; Satellite-derived cloud effective radius (*CER*, c) and cloud optical thickness (*COT*, d) in 1 June to 30 July 2019.

Fig. S2 Sampling system diagram. 1-Intake pipe, 2-Drying tube, 3-CPC, 4-FMPS, 5-CCNC, 6-DMA, 7-NAS, 8-Air outlet.

Fig. S3 Contour plots of an NPF event measured simultaneously by the FMPS (a) and SMPS (b) on 29 June 2019, and the comparison of $N_{10–200}$ (c) and D_p (d) of grown new particles measurements obtained from both instruments at a 4-minute time resolution.

Fig. S4 The comparison of $N_{10–200}$ measured simultaneously by the SMPS and WPS, conducted from 2 July 2020 to 7 July 2020 (a). The comparison of N measured simultaneously using two different CPCs, conducted from 25 August 2021 to 26 August 2021. CPC-1, which was used in this study, was compared to CPC-2 from the Jilin Provincial Meteorological Bureau (b).

Fig. S5 The correlation between N_{ccn} at 0.2 % SS and $N_{cn>100}$.

Fig. S6 N_{ccn} observed at various SS levels on 16 observational days. The solid and dashed lines represent the top and bottom fitting lines and those between.

Fig. S7 The contour plots of particle number size distribution, time series for $N_{cn>100}$, and time series for N_{ccn}, κ values and D_{crit} at the lab-calibrated SS and the corresponding on-site approximated values on 12–14 July.

Fig. S8 The contour plots of particle number size distribution on no-NPF days. (2 July (a), 4 July (b), 5 July (c), 7 July (d), 8 July (e), 9 July (f), 10 July (g), 11 July (h)).

Fig. S9 Time series of κ values at 1.0 % on 29 June, 3 July and 6 July.

Fig. S10 ToF-SIMS spectral comparison of atmospheric nanometer particles collected on 30 June (a) and 1 July 2019 (b) in the positive ion mode (m/z^+ 0–200).

Fig. S11 ToF-SIMS spectral comparison of atmospheric nanometer particles collected on 30 June (a) and 1 July 2019 (b) in the negative ion mode (m/z^- 0–200).

Fig. S12 ToF-SIMS spectral comparison of atmospheric nanometer particles collected on 30 June (a) and 1 July 2019 (b) in the negative ion mode (m/z^- 200–350).

Fig. S13 ToF-SIMS selected peak spectral PCA results of 60, 100, and 200 nm particles on 30 June (gray markers) as well as 30 nm, 60 nm, 100 nm, and 200 nm particles on 1 July (red markers) in the negative mode: Scores plots of PC1 vs. PC2 (a), PC1 loadings plots in m/z^- 30–550 (b), and PC2 loading plots in m/z^- 30–550 (c). Peaks are labelled in their center masses.

Table legend:

Table S1. Number concentrations of CN and CCN on NPF days or non-NPF days.

Supplementary text

S1 Operational details of experiments

S1.1 Gas chromatography mass spectroscopy

Measure organic tracers using a gas chromatography mass spectroscopy with an Agilent 6890 GC/5975 MSD. The analyzing procedure was adapted from Kleindienst et al. (2007) and Feng et al. (2013). Briefly, 20mL dichloromethane/methanol (1:1, v/v) was used to extract ultrasonically 25 cm^2 of each quartz filter three times at room temperature, and the extracts combined. The extracts were filtered, dried and then derivatized with 100 μL N, O-bis-(trimethylsilyl)-trifluoroacetamide (BSTFA, containing 1 % trimethylchlorosilane as a catalyst) and 20 μL pyridine at 75 ℃ for 45 min. Surrogate mixture of methylb-D-xylanopyranoside (MXP) and cis-ketopinic acid (KPA) were spiked into the samples as internal/recovery standards before the extraction. Before the injection, hexamethylbenzene was added as an internal standard to check the recovery of the surrogates.

S1.2 Ion chromatography

The operation details of ion chromatography mainly refer to Hu et al. (2015) and Teng et al. (2017). The ion chromatography (Dionex 3000) was used to analyze he inorganic ions in TSP samples. The samples were ultrasonically extracted in deionized water (18 MΩ•cm) at 0 ℃ for 20 min. The extracts were filtered through a prebaked Whatman GF/F glass fiber filter and then injected to the ion chromatograph equipping with different analytical columns for ion analysis.

S2 Calculation methods

S2.1 Apparent new particle formation rate (FR)

$$FR = \frac{dN_{[d_k,d_u)}}{dt} + \sum_{d_g=d_k}^{d_{u-1}} \sum_{d_i=d_{min}}^{+\infty} \beta_{(i,g)} N_{[d_i,d_{i+1})} - \frac{1}{2} \sum_{d_g=d_{min}}^{d_{u-1}} \sum_{d_i^3=max(d_{min}^3, d_k^3-d_{min}^3)}^{d_{i+1}^3+d_g^3 \le d_u^3} \beta_{(i,g)} N_{[d_i,d_{i+1})} N_{[d_g,d_{g+1})} + n_u \cdot GR_u \quad \text{(S1)}$$

Where FR is the particle formation rate at size d_k, $cm^3\ s^{-1}$, (7 nm in this study); d_u is the upper size limit of the targeted aerosol population (10 nm in this study); d_{min} is the smallest particle size detected by particle size spectrometers (to make the results comparable, the d_{min} was set to 7 nm); $N_{[dk,du)}$ is the number

concentration of particles from size d_k to d_u; d_i represents the lower limit of the size bin; $\beta_{(i,g)}$ is the coagulation coefficient for the collision of two particles with the size of d_i and d_g; and GR_u refers to the particle growth rate at size d_u, nm h^{-1}

S2.2 Net maximum increase in the nucleation-mode particle number concentration (NMINP)

$$NMINP = N_{<30}(t_1) - N_{<30}(t_0) \quad \text{(S2)}$$

Where $N_{<30}$ is the sum of nucleation mode particle number concentrations, and t_0 and t_1 represent the time of an NPF event to be initially observed and the time when $N_{<30}$ reaches the maximum value, respectively.

S2.3 Multi-lognormal distribution functions

$$f(D_p, D_{pg,i}, C_i, \sigma_{g,i}) = \sum_{i=1}^{n} \frac{C_i}{(2\pi)^{1/2} log_{(\sigma_{g,i})}} \times exp[-\frac{[log(D_p) - log(D_{pg,i})]^2}{2log^2(\sigma_{g,i})}] \quad \text{(S3)}$$

Where D_p is the diameter of aerosol particle. Three parameters characterize an individual lognormal mode i: the mode number concentration, C_i, geometric variance, and $\sigma_{g,i}^2$, geometric mean diameter $D_{pg,i}$. The number of individual lognormal modes that characterize the particle number size distribution is denoted by n (i is in the range of 1–n). In this study, n is usually equal to 2, and $D_{pg,i}$ represents the geometric median diameter of new particles followed by particle growth in the observed events. The growth of pre-existing Aitken mode particles was also observed in this study, and $D_{pg,2}$ represents the geometric median diameter of the pre-existing particles. And the corresponding half width (standard deviation, σ) in 99.7 % confidence was calculated by:

$$\sigma = 10^{3log(\sigma_{g,i})} \quad \text{(S4)}$$

S3 Inter-comparison of particle number concentration related instruments

Four different instruments related to particle number concentration were installed on the third floor of the station's major building, at a height of 10 m above ground (Fig. S2). These instruments included a Fast Mobility Particle Sizer (FMPS, TSI, 3091) downstream of a dryer (TSI, 3062), a Condensation Particle Counter (CPC, TSI, 3775), a continuous flow CCN counter (CCNC, DMT Model 100), and a Differential Mobility Analyzer (DMA, Grimm) coupled with a Nanometer Aerosol Sampler (NAS, Grimm). The FMPS had undergone maintenance at the TSI factory in the U.S. before the campaign, and

the ratios of the measured total particle number concentrations measured by the FMPS against those measured by the CPC remained stable until the end of 2021. Moreover, the particle number size distributions (*PNSD*) measured by the FMPS were corrected using the data simultaneously measured by the CPC according to the well-established approach in the literature. The accuracy of the total particle number concentrations measured by the CPC was critical for this correction. The accuracy of CPC was also examined after the campaign because of lack of two identical CPC during the campaign.

Figure S3 showed contour plots of an NPF event measured simultaneously by the FMPS and the SMPS on 29 June 2019, in which the spectra are reasonably consistent. For example, the $N_{10–200}$ measured by the two sizers is highly correlated with $N_{10–200\text{-}FMPS} = 2.5 \times N_{10–200\text{-}SMPS}$, $R^2 = 0.92$. However, the SMPS suffered from the particle diffusion loss to some extent. In addition, they measured the reasonably consistent D_p of grown new particles, i.e., $D_{p\text{-}FMPS} = 1.02 \times D_{p\text{-}SMPS} - 4.6$, $R^2 = 0.85$. An inter-comparison between the SMPS and a wide-range particle sizer after the campaign also confirmed the same particle diffusion loss in the SMPS (Fig. S4a). After the campaign, an inter-comparison between the CPC, referred as CPC-1, and another identical CPC, referred as CPC-2, showed that $N_{cn\text{-}CPC2} = 1.05 \times N_{cn\text{-}CPC1}$, $R^2 = 0.995$ (Fig. S4b). The comparison further confirmed the accuracy of the CPC measurements.

N_{ccn} at 0.2 % SS and $N_{cn>100}$ was reasonably consistent during the whole campaign (Fig. S5), especially at lower number concentrations. For example, $N_{ccn(0.2\%)} = 0.83 \times N_{cn>100} - 85$, $R^2 = 0.66$ and $p < 0.05$, when $N_{cn>100}$ was smaller than 1000 cm^{-3}. In fact, an even stronger correlation between N_{ccn} at 0.2 % SS and $N_{cn>100}$ during some short periods as presented in the text, e.g., a significant correlation existed between N_{ccn} and $N_{cn>100}$ from 10:00 to 14:00 on 30 June 2019, with an equation of $N_{ccn} = N_{cn>100} \times 1.42 - 5.6 \times 10^2$, $R^2 = 0.83$, and $p < 0.05$ at 0.2 % SS. Moreover, the variations in N_{ccn} at 0.2 % SS were likely determined by the number concentrations of larger pre-existing particles based on the correlation between N_{ccn} at 0.2 % SS and $N_{cn>100}$ from 09:00 to 24:00 on 29 June. The regression equation can be expressed as follows: $N_{ccn} = N_{cn>100} \times 0.42 + 64$, with an R^2 of 0.70 and $p < 0.01$, at 0.2 % SS. However, the data points appeared to be largely and negatively deviated from the regression curve at $N_{cn>100}$ exceeding 3000 cm^{-3} (Fig. S5). The large deviation with increasing $N_{cn>100}$ is not surprised by considering an increasing contribution of $N_{cn>100}$ from various primary sources.

S4 Artifact analysis of N_{ccn} and κ values at lab-calibrated SS and approximated on-site SS

Rose et al. (2008) reported that a 10 % decrease in atmospheric pressure led to an approximately 10 % reduction in supersaturation (SS). The divergence in height between the observational site and the calibration location (~1000 m) may introduce uncertainties on SS and the consequently measured N_{ccn} (Lance et al., 2006; Rose et al., 2008; Lathem and Nenes, 2011). Based on the results in the literature, i.e., Eq. (16) in Lance et al., 2006; Fig. 5d and Fig. 8c in Rose et al., 2008, the on-site five SS at the mountain site might be 0.18 %, 0.36 %, 0.54 %, 0.72 % and 0.9 % SS, corresponding to the lab-calibrated 0.2 %, 0.4 %, 0.6 %, 0.8 % and 1.0 % SS, respectively. These smaller SS values were referred as the approximated on-site values in this study. Furthermore, the errors in the measured N_{ccn} between each pair of the lab-calibrated and approximated on-site SS were found to be smaller than 10 %, as presented below.

Considering that N_{ccn} can be expressed as a function of SS, i.e., so-called Twomey expression, i.e., $N_{ccn,SS} = C \times SS^k$, where C and k are two constants (Twomey, 1959; Ji and Shaw, 1998). The exponential function was used to fit the observed N_{ccn} at SS ranging from 0.2 % to 1.0 % during the 16 days in this study (Fig. S6). A good correlation can be obtained with $R^2 = 0.97 \pm 0.05$, although the C and k varied a lot because of different types of aerosols to be measured.

In each day, the obtained fitting equation was used to calculate N_{ccn} at 0.18 %, 0.36 %, 0.54 %, 0.72 % and 0.9 % SS. This allowed us to estimate the errors in N_{ccn} at each pair of lab-calibrated and approximated on-site SS. For example, on 2 July and 6 July when the highest and lowest N_{ccn} were observed, the relative errors between 0.18 % and 0.2 % SS were 3 % and 4 %, respectively. The largest relative errors of 6 % between 0.18 % and 0.2 % SS were obtained on 30 June. Between 0.36 % and 0.4 % SS, the relative errors of N_{ccn} were 2 % on 2 July and 3 % on 6 July, with the highest value of 9 % on 8 July. Importantly, all errors remained within 10% at various SS levels. Additionally, the relative errors on NFP-days and non-NPF days were calculated separately. Between 0.18 % and 0.2 % SS, the errors were 3 % ± 2 % on NPF days, and 4 % ± 1 % on non-NPF days. These small errors had a negligible impact on our analysis through the study.

To compare with κ values at the lab-calibrated SS, the corresponding κ values at the approximated on-site SS on 29 June, 30 June, 1 July, and 6 July were illustrated in Figs. 3–5. For example, on 1 July, the relative errors of κ value were 23 % ± 14 % between 0.18 % and 0.2 % SS, and 34 % ± 32 % between

0.36 % and 0.4 % SS. More results had been included in the main text for clarifying the possible influence of the errors on the analyses associated.

Reference

Kleindienst, T. E., Jaoui, M., Lewandowski, M., Offenberg, J. H., Lewis, C. W., Bhave, P. V., and Edney, E. O.: Estimates of the contributions of biogenic and anthropogenic hydrocarbons to secondary organic aerosol at a Southeastern US location, Atmos. Environ., 41, 8288–8300, https://doi.org/10.1016/j.atmosenv.2007.06.045, 2007.

Feng, J., Li, M., Zhang, P., Gong, S., Zhong, M., Wu, M., Zheng, M., Chen, C., Wang, H., and Lou, S.: Investigation of the sources and seasonal variations of secondary organic aerosols in PM2.5 in Shanghai with organic tracers, Atmos. Environ., 79, 614–622, https://doi.org/10.1016/j.atmosenv.2013.07.022, 2013.

Hu, Q., Li, K., Zhu, Y., Yu, P., Gao, H., and Yao, X.: Concentration, size distribution, and formation of trimethylaminium and dimethylaminium ions in atmospheric particles over marginal seas of China, J. Atmos. Sci., 72, 3487–3498, https://doi.org/10.1175/jas-d-14-0393.1, 2015.

Teng, X., Hu, Q., Zhang, L., Qi, J., Shi, J., Xie, H., Gao, H., and Yao, X.: Identification of major sources of atmospheric NH3 in an urban environment in Northern China during wintertime, Environ. Sci. Technol., 51, 6839–6848, https://doi.org/10.1021/acs.est.7b00328, 2017.

Lance, S., Nenes, A., Medina, J., and Smith, J. N.: Mapping the operation of the 20 DMT continuous flow CCN counter, Aerosol Sci. and Technol., 40, 242–254, https://doi.org/10.1080/02786820500543290, 2006.

Rose, D., Gunthe, S. S., Mikhailov, E., Frank, G. P., Dusek, U., Andreae, M. O., and Pöschl, U.: Calibration and measurement uncertainties of a continuous-flow cloud condensation nuclei counter (DMT-CCNC): CCN activation of ammonium sulfate and sodium chloride aerosol particles in theory and experiment, Atmos. Chem. Phys., 8, 1153–1179, https://doi.org/10.5194/acp-8-1153-2008, 2008.

Lathem, T. L. and Nenes, A.: Water vapor depletion in the DMT continuous-flow CCN chamber: Effects on supersaturation and droplet growth, Aerosol Sci. and Technol., 45, 604–615, https://doi.org/10.1080/02786826.2010.551146, 2011.

Twomey, S.: The nuclei of natural cloud formation part II: the supersaturation in natural clouds and th e variation of cloud droplet concentration. Pure. Appl. Geophys., 43, 243–249, https://doi.org/10.1 007/BF01993560, 1959.

Ji, Q. and Shaw, G. E.: On supersaturation spectrum and size distributions of cloud condensation nucle i, Geophys. Res. Lett., 25, 1903–1906, https://doi.org/10.1029/98gl01404, 1998.

Figures

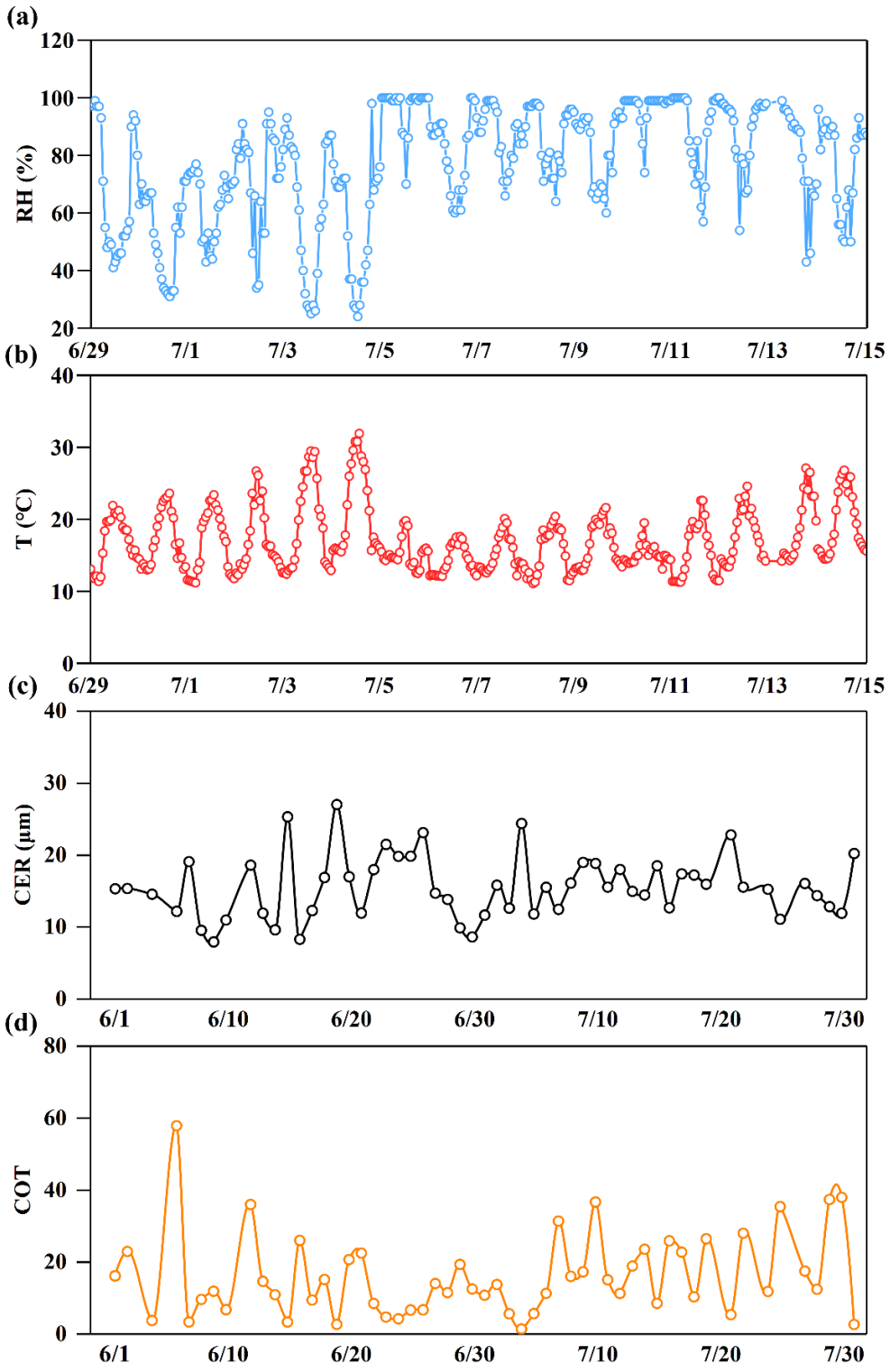

Fig. S1 Temporal variations in relative humidity (RH, a) and temperature (T, b) from 29 June to 15 July 2019; Satellite-derived cloud effective radius (*CER*, c) and cloud optical thickness (*COT*, d) in 1 June to 30 July 2019.

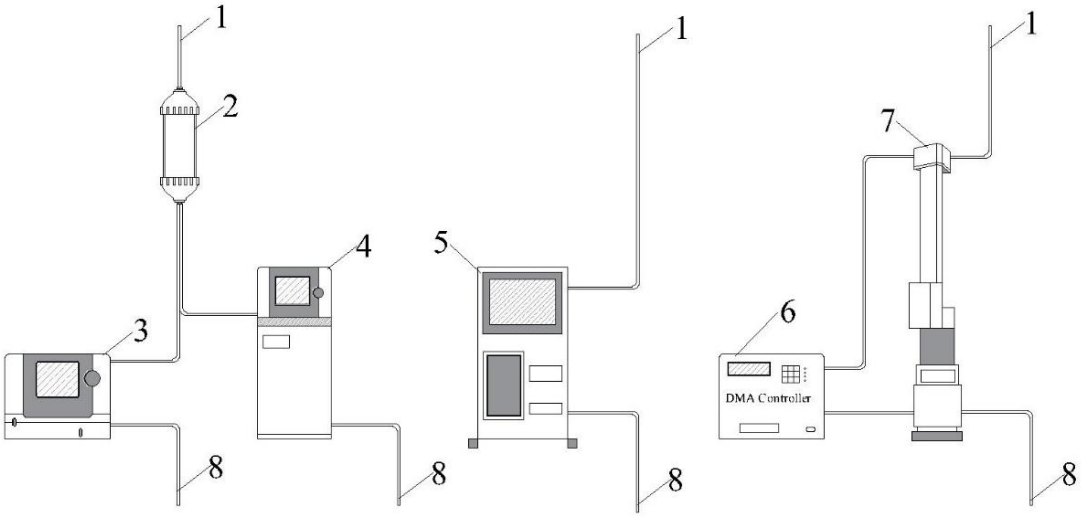

Fig. S2 Sampling system diagram. 1-Intake pipe, 2-Drying tube, 3-CPC, 4-FMPS, 5-CCNC, 6-DMA, 7-NAS, 8-Air outlet.

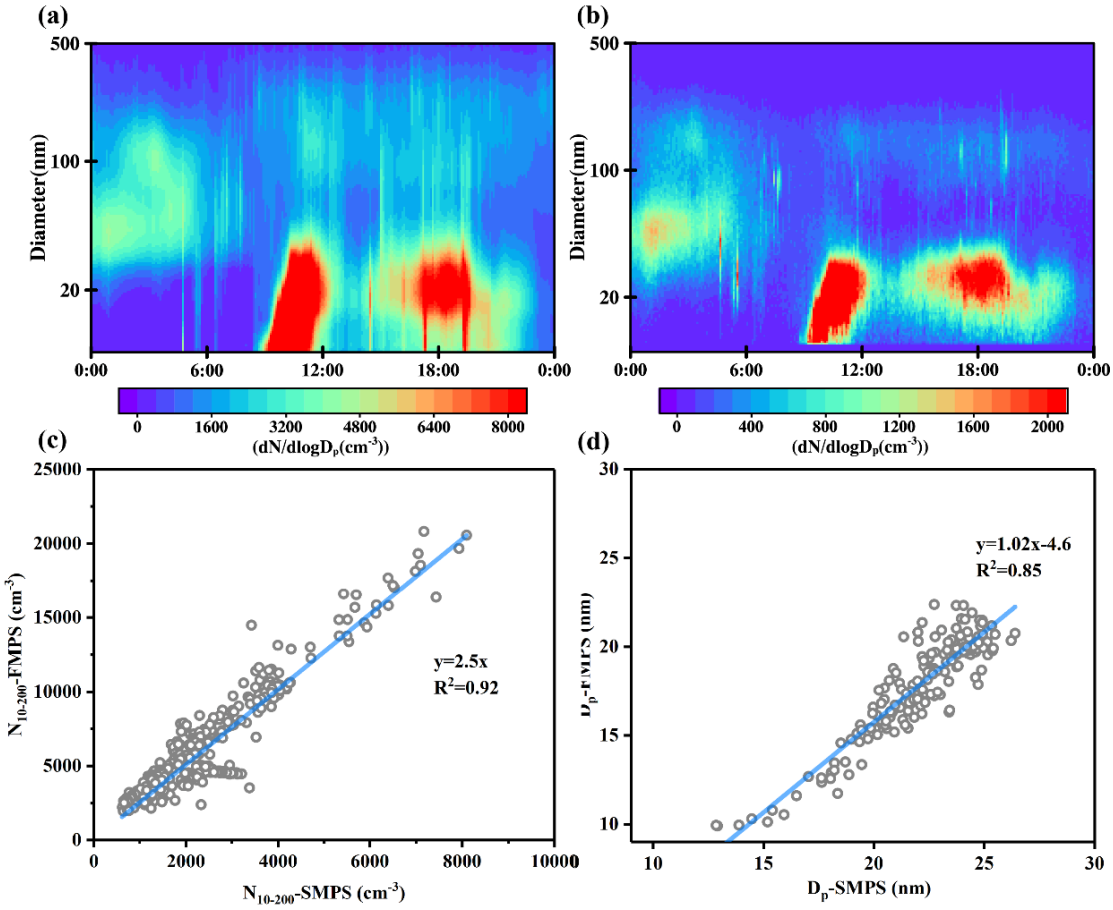

Fig. S3 Contour plots of an NPF event measured simultaneously by the FMPS (a) and SMPS (b) on 29 June 2019, and the comparison of $N_{10–200}$ (c) and D_p (d) of grown new particles measurements obtained from both instruments at a 4-minute time resolution.

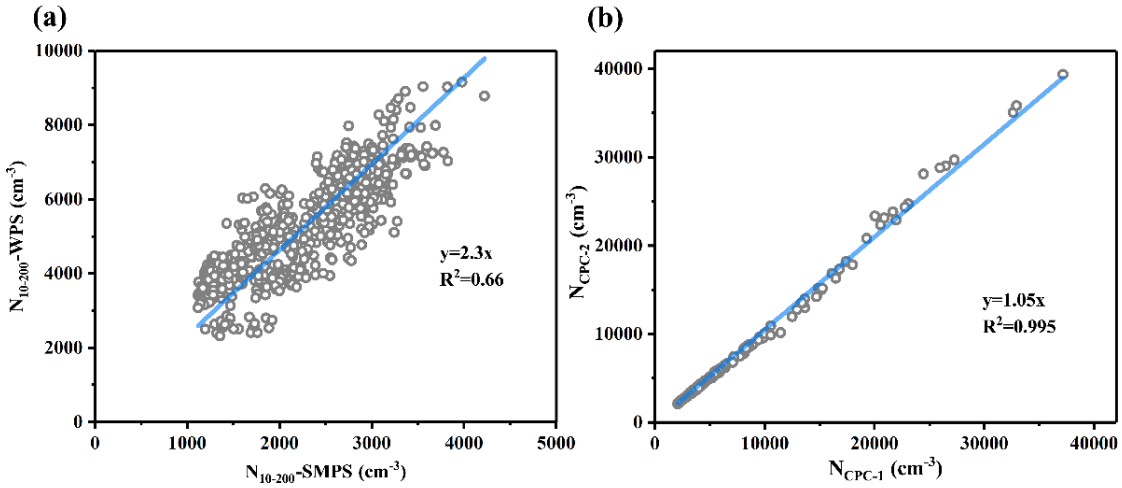

Fig. S4 The comparison of $N_{10–200}$ measured simultaneously by the SMPS and WPS, conducted from 2 July 2020 to 7 July 2020 (a). The comparison of N measured simultaneously using two different CPCs, conducted from 25 August 2021 to 26 August 2021. CPC-1, which was used in this study, was compared to CPC-2 from the Jilin Provincial Meteorological Bureau (b).

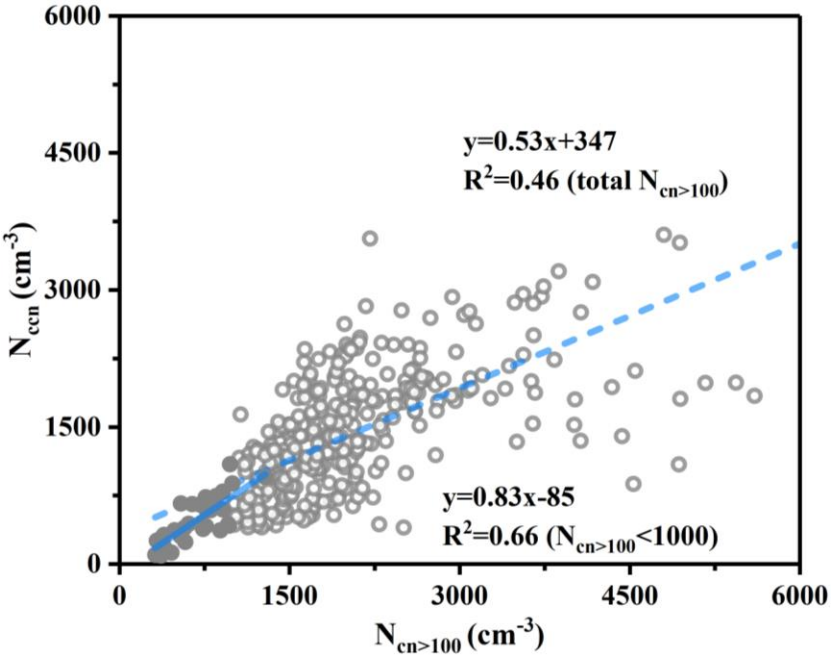

Fig. S5 The correlation between N_{ccn} at 0.2 % SS and $N_{cn>100}$.

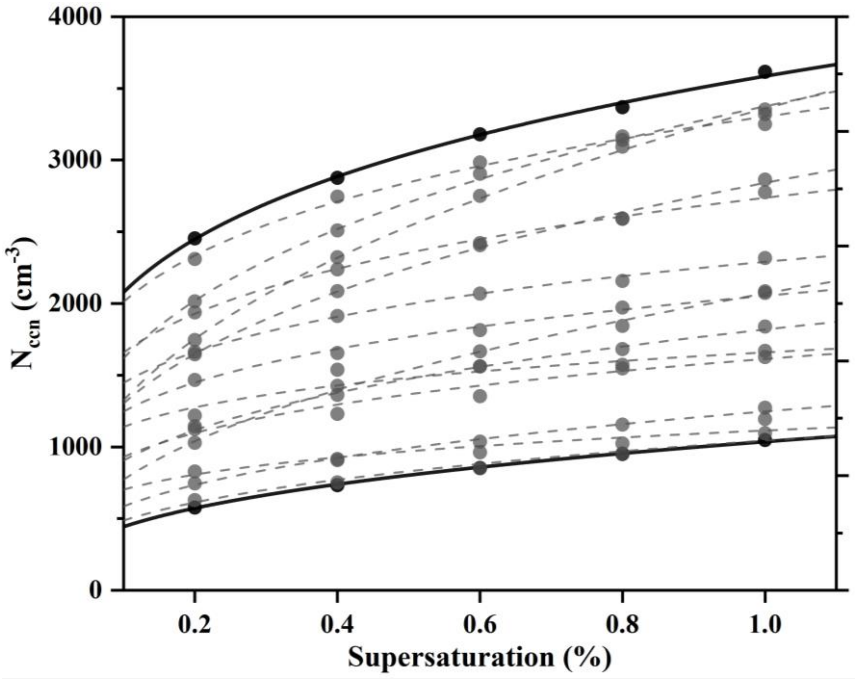

Fig. S6 N_{ccn} observed at various SS levels on 16 observational days. The solid and dashed lines represent the top and bottom fitting lines and those between.

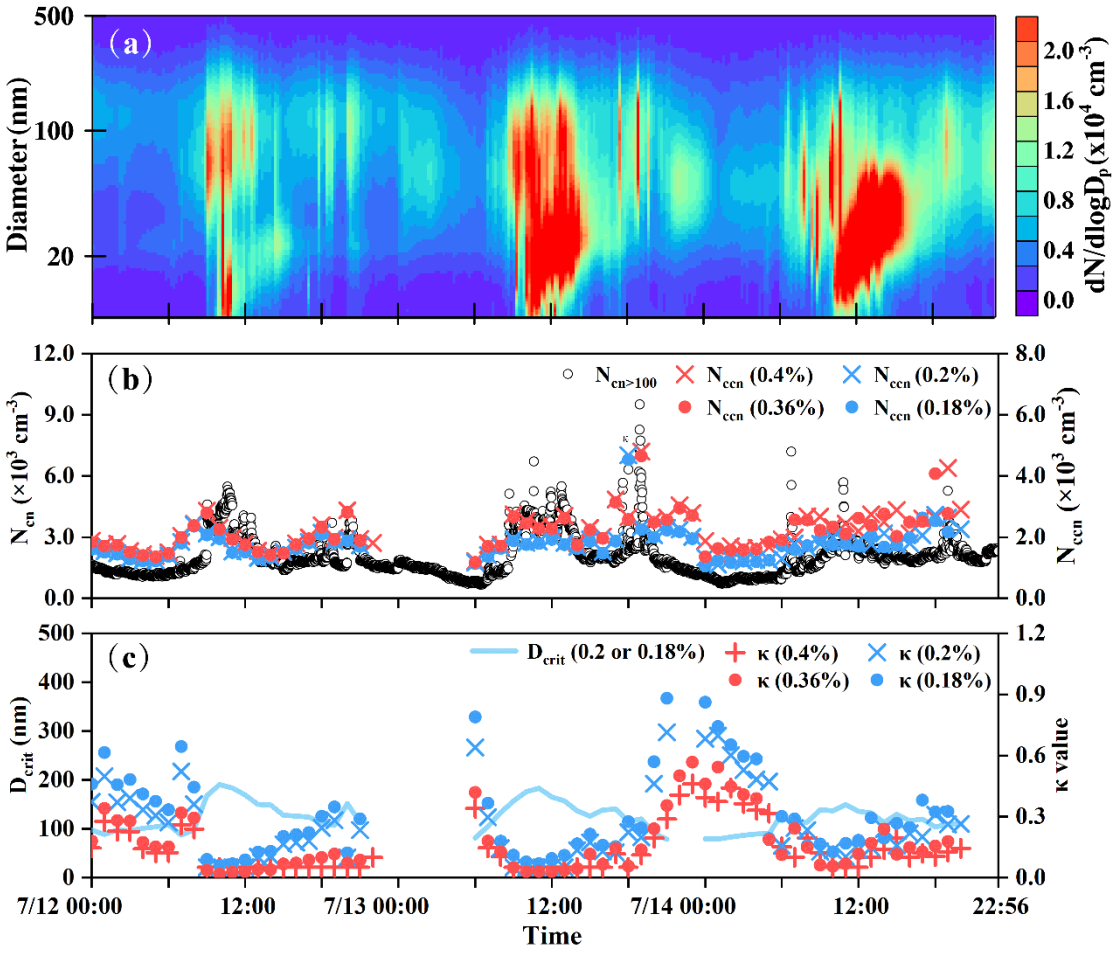

Fig. S7 The contour plots of particle number size distribution, time series for $N_{cn>100}$, and time series for N_{ccn}, κ values and D_{crit} at the lab-calibrated SS and the corresponding on-site approximated values on 12–14 July.

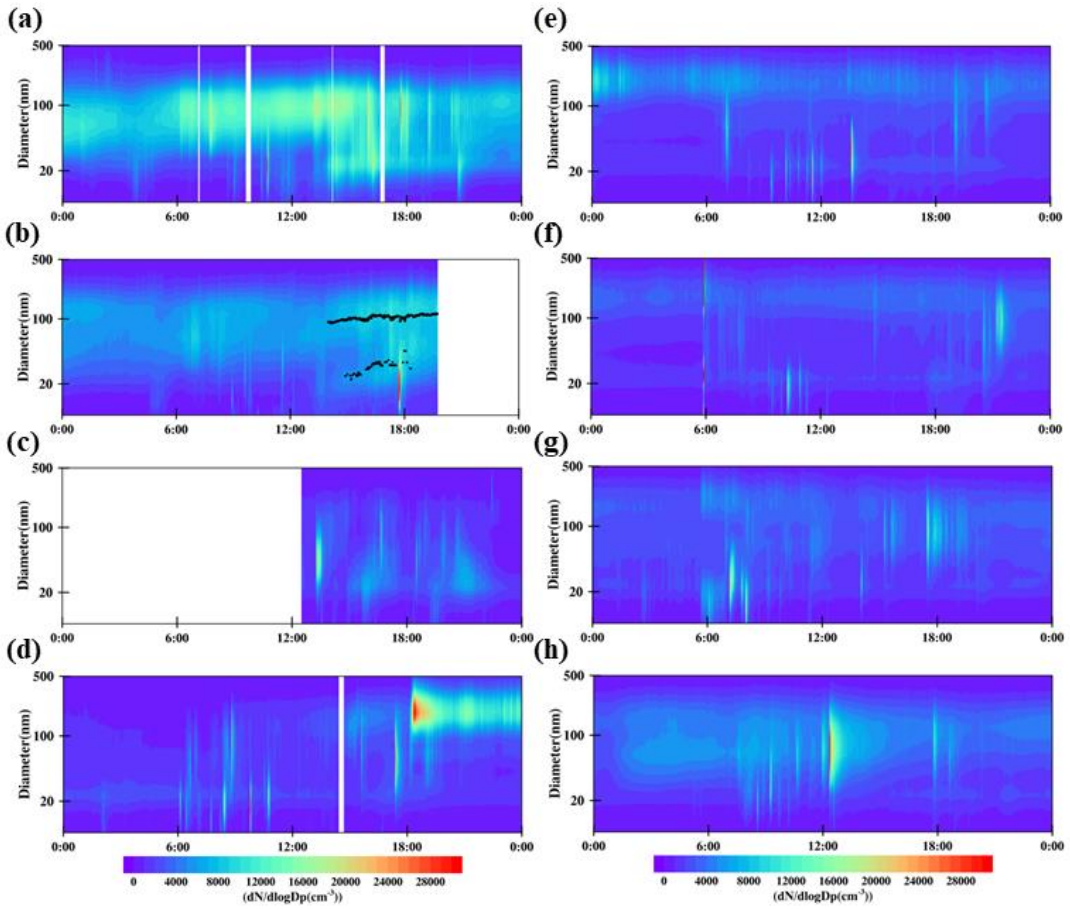

Fig. S8 The contour plots of particle number size distribution on no-NPF days. (2 July (a), 4 July (b), 5 July (c), 7 July (d), 8 July (e), 9 July (f), 10 July (g), 11 July (h)).

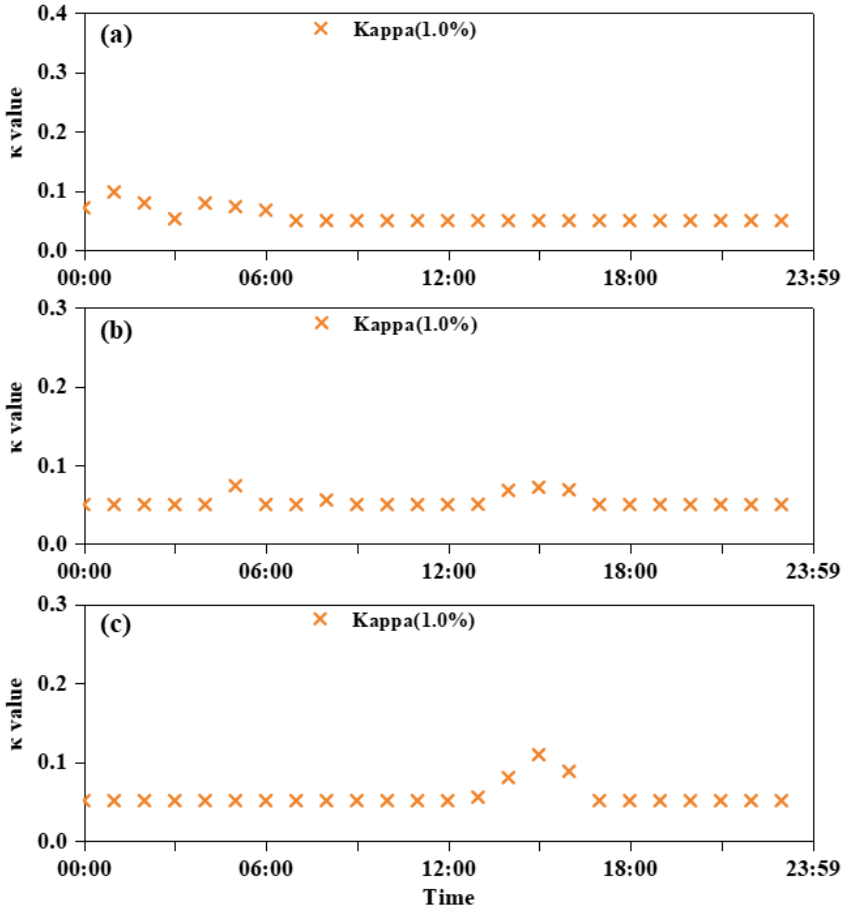

Fig. S9 Time series of *κ* values at 1.0 % on 29 June, 3 July and 6 July.

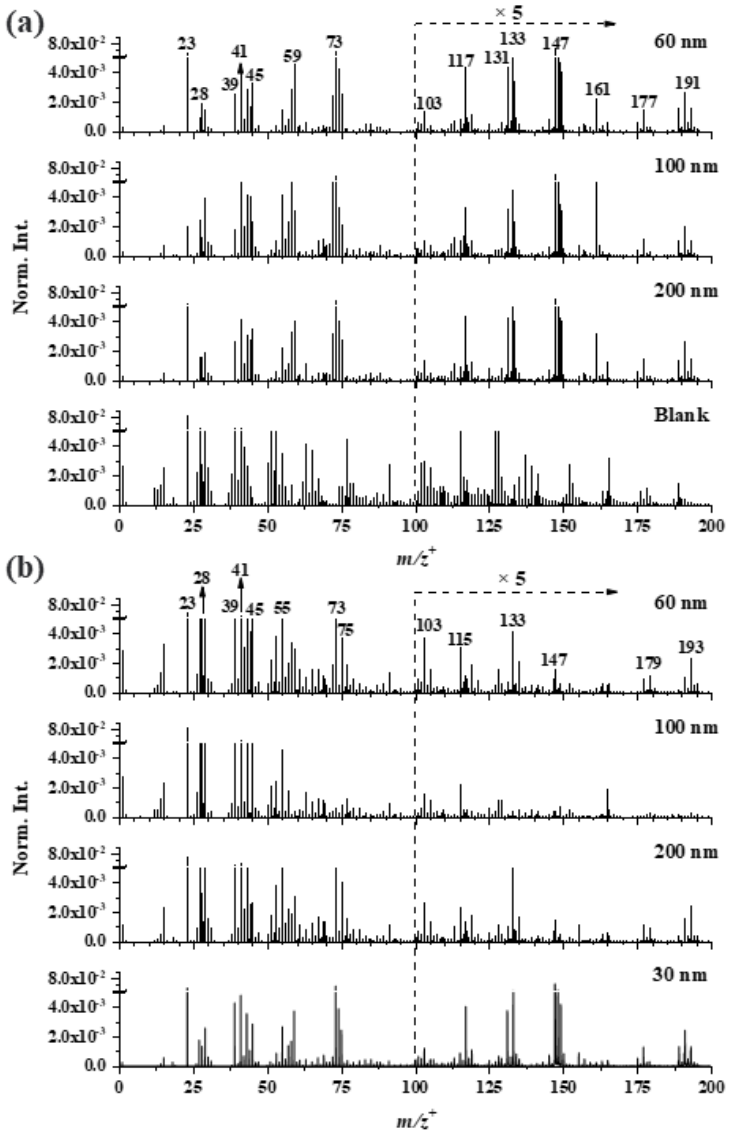

Fig. S10 ToF-SIMS spectral comparison of atmospheric nanometer particles collected on 30 June (a) and 1 July 2019 (b) in the positive ion mode (m/z^+ 0–200).

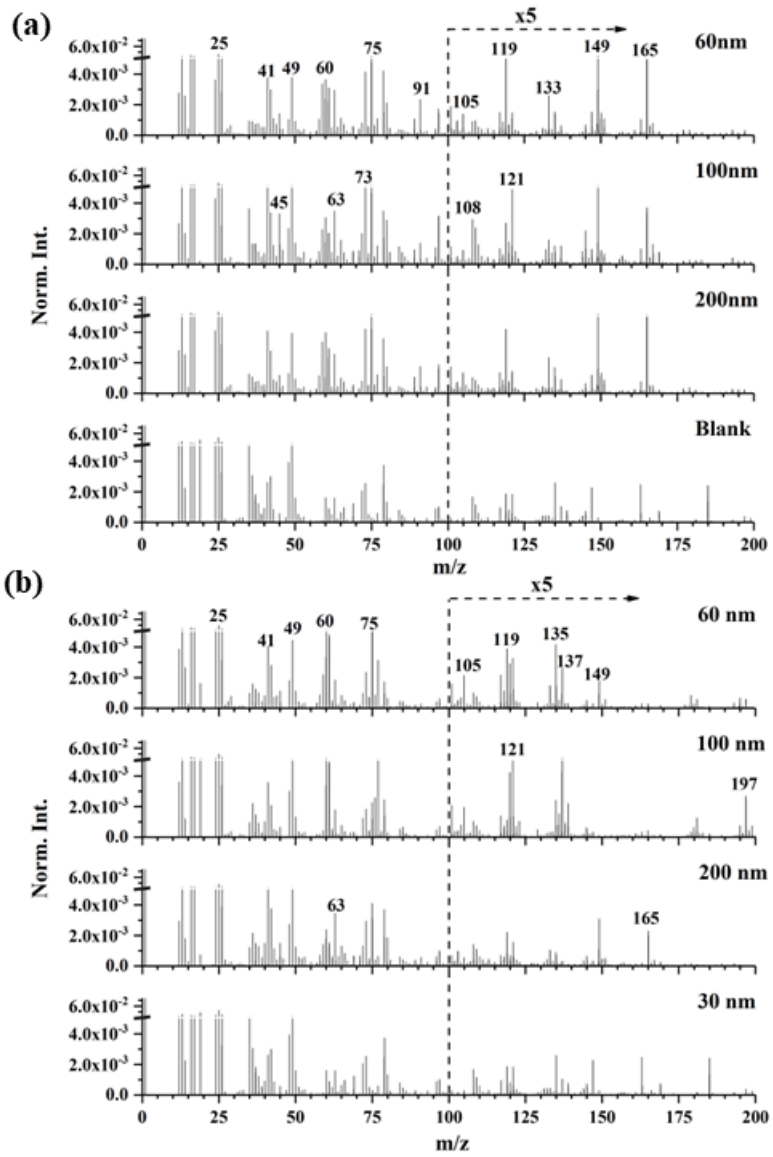

Fig. S11 ToF-SIMS spectral comparison of atmospheric nanometer particles collected on 30 June (a) and 1 July 2019 (b) in the negative ion mode (*m/z*$^+$ 0–200).

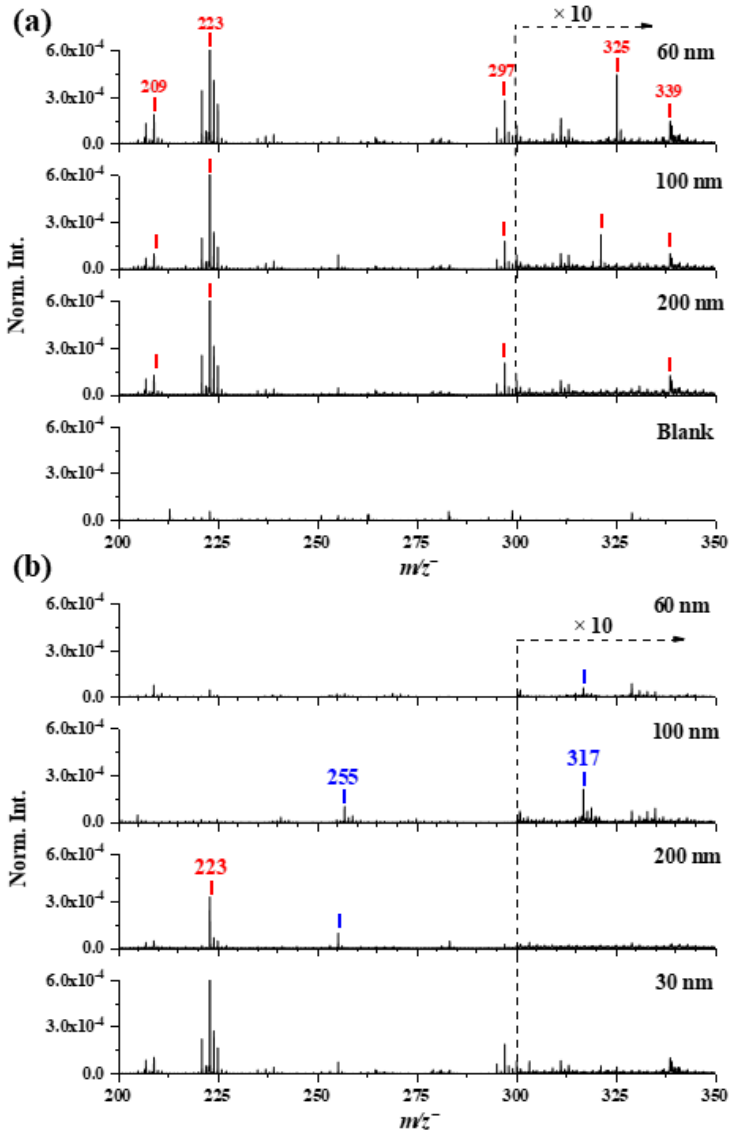

Fig. S12 ToF-SIMS spectral comparison of atmospheric nanometer particles collected on 30 June (a) and 1 July 2019 (b) in the negative ion mode (*m/z*⁻ 200–350).

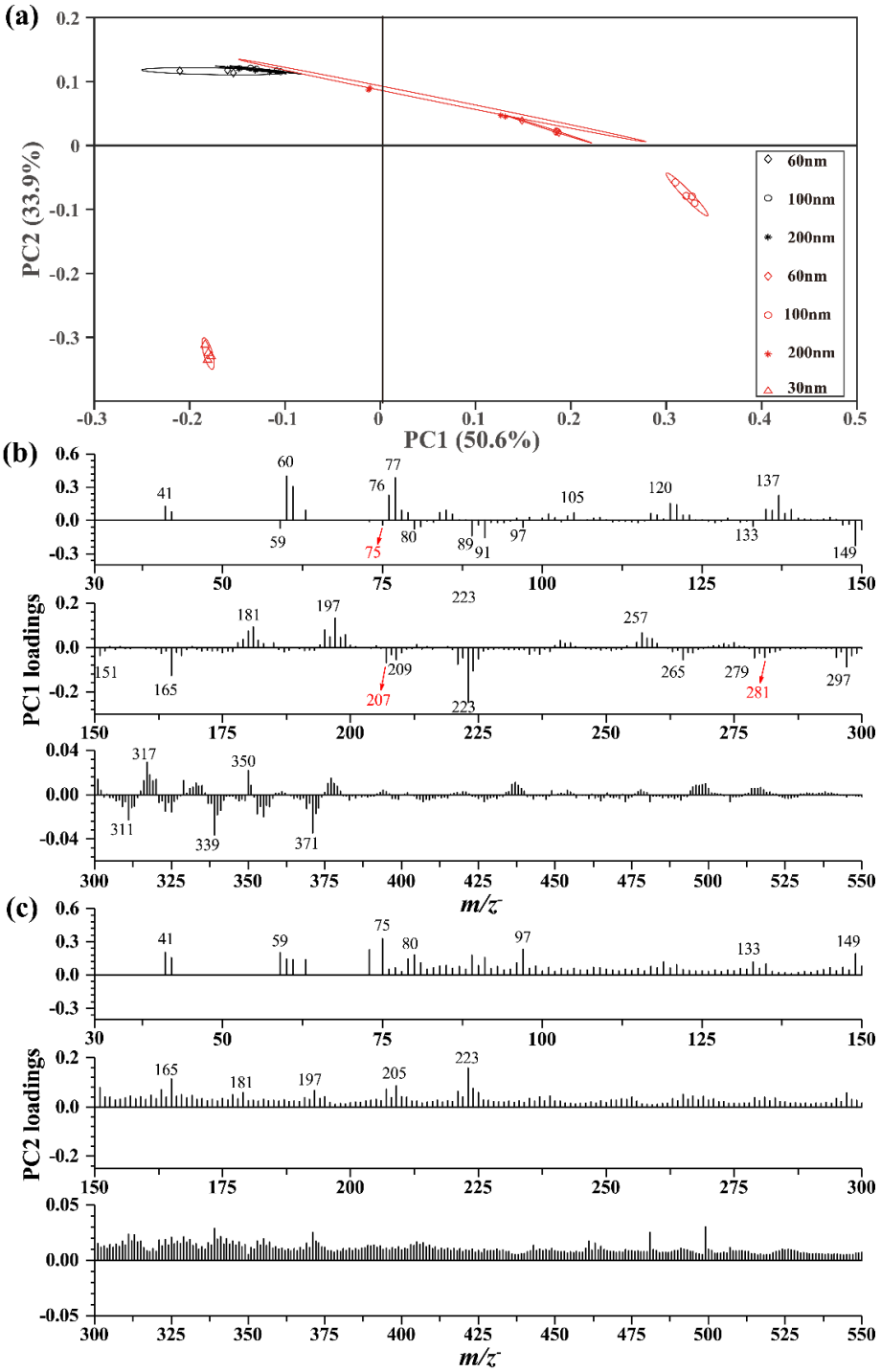

Fig. S13 ToF-SIMS selected peak spectral PCA results of 60, 100, and 200 nm particles on 30 June (gray markers) as well as 30 nm, 60 nm, 100 nm, and 200 nm particles on 1 July (red markers) in the negative mode: Scores plots of PC1 vs. PC2 (a), PC1 loadings plots in m/z^- 30–550 (b), and PC2 loading plots in m/z^- 30–550 (c). Peaks are labelled in their center masses.

Table

Table S1. Number concentrations of CN and CCN on NPF days or non-NPF days.

	Date	N_{ccn} at five SS levels					$N_{cn>100}$	Total N_{cn}
		0.2 %	0.4 %	0.6 %	0.8 %	1.0 %		
NPF days	June 29	0.7 ± 0.3 [a,b]	0.9 ± 0.4	1.0 ± 0.5	1.2 ± 0.6	1.3 ± 0.6	1.3 ± 0.4	7.5 ± 4.3
	June 30	0.6 ± 0.2	0.7 ± 0.2	0.9 ± 0.3	1.0 ± 0.4	1.1 ± 0.6	1.4 ± 0.6	7.4 ± 4.5
	July 1	1.0 ± 0.5	1.4 ± 0.8	1.7 ± 1.0	1.9 ± 1.1	2.1 ± 1.3	1.3 ± 0.3	8.2 ± 5.3
	July 3	1.6 ± 0.5	2.0 ± 0.7	2.3 ± 0.8	2.5 ± 0.8	2.8 ± 0.8	2.0 ± 0.6	9.4 ± 3.2
	July 6	0.6 ± 0.3	0.7 ± 0.4	0.9 ± 0.6	1.0 ± 0.7	1.1 ± 0.8	0.8 ± 0.3	7.5 ± 7.8
	July 12	1.6 ± 0.5	1.8 ± 0.6	1.9 ± 0.8	2.0 ± 0.8	2.2 ± 1.0	2.0 ± 0.9	6.5 ± 4.5
	July 13	1.5 ± 1.2	1.8 ± 1.4	2.1 ± 1.6	2.3 ± 1.7	2.5 ± 1.8	2.1 ± 1.1	10.0 ± 7.6
	July 14	1.7 ± 0.5	2.3 ± 0.8	2.8 ± 0.8	3.1 ± 1.2	3.3 ± 1.2	1.9 ± 1.1	11.0 ± 8.2
	Avg	1.2 ± 0.7	1.5 ± 0.9	1.7 ± 1.1	1.9 ± 1.2	2.1 ± 1.2	1.6 ± 0.8	8.4 ± 6.1
Non-NPF days	July 2	2.4 ± 0.6	2.9 ± 0.6	3.2 ± 0.7	3.4 ± 0.7	3.6 ± 0.8	1.8 ± 0.5	6.1 ± 1.6
	July 4	2.3 ± 0.4	2.7 ± 0.4	3.0 ± 0.4	3.2 ± 0.5	3.3 ± 0.5	2.0 ± 0.5	6.2 ± 1.8
	July 5	1.1 ± 0.9	1.4 ± 1.0	1.6 ± 1.0	1.7 ± 1.1	1.8 ± 1.1	0.6 ± 0.3	3.0 ± 1.4
	July 7	0.8 ± 0.5	0.9 ± 0.5	1.0 ± 0.4	1.1 ± 0.6	1.2 ± 0.6	1.8 ± 2.1	3.6 ± 2.4
	July 8	1.2 ± 0.3	1.5 ± 1.0	1.5 ± 0.7	1.5 ± 0.5	1.6 ± 0.5	1.7 ± 0.4	3.3 ± 1.2
	July 9	1.1 ± 0.7	1.2 ± 0.5	1.4 ± 0.7	1.6 ± 1.2	1.7 ± 1.8	1.4 ± 0.8	3.2 ± 1.8
	July 10	1.5 ± 0.6	1.6 ± 0.6	1.8 ± 0.6	2.0 ± 0.8	2.1 ± 1.0	1.7 ± 0.7	4.5 ± 2.1
	July 11	1.9 ± 0.3	2.2 ± 0.4	2.4 ± 0.5	2.6 ± 0.6	2.8 ± 0.9	1.8 ± 0.4	4.8 ± 1.4
	Avg	1.6 ± 0.8	1.8 ± 0.9	2.0 ± 1.0	2.1 ± 1.1	2.3 ± 1.1	1.7 ± 1.0	4.4 ± 2.1

a. Unit in $\times 10^3$ cm^{-3}.

b. average ± standard deviation.